Anthraquinone-Based Silicate Covalent Organic Frameworks as Solid Electrolyte Interphase for High-Performance Lithium-Metal Batteries

Yoonseob Kim (yoonseobkim@ust.hk)
HKUST https://orcid.org/0000-0002-6892-8281
Chen Li
The Hong Kong University of Science & Technology
Dan-dong Wang
Shanghai Jiao Tong University
Gerald Siu Hang Poon Ho
The Hong Kong University of Science & Technology
Zhengyang Zhang
Shanghai Jiao Tong University
Jun Huang
The Hong Kong University of Science & Technology
Ki-Taek Bang
The Hong Kong University of Science & Technology
Chun Yin Lau
The Hong Kong Polytechnic University
Shao-Yuan Leu
The Hong Kong Polytechnic University
Yanming Wang
Shanghai Jiao Tong University https://orcid.org/0000-0002-0912-681X

Article

Keywords: Covalent organic frameworks, Li-metal batteries, Solid electrolyte interphase, Redox activity

Posted Date: June 21st, 2023

DOI: https://doi.org/10.21203/rs.3.rs-2671248/v1

Abstract

Lithium (Li)-metal batteries (LMBs) have the highest theoretical energy density of current battery designs and thus have enormous potential for use in energy storage. However, the safety problems caused by dendrite growth and unstable interphases on the Li anode severely impede their development. Covalent organic frameworks (COFs) containing either redox-active or anionic moieties on their backbones have high Li-ion (Li^+) conductivities and mechanical/chemical stabilities, so are promising for solid-electrolyte interphases in LMBs. Here, we synthesized anthraquinone-based silicate COFs (AQ-Si-COFs) that contained both redox-active and anionic sites via condensation of tetrahydroxy-anthraquinone with silicon dioxide. The nine Li^+ mediated charge/discharge processes enabled the AQ-Si-COF to demonstrate a Li^+ conductivity of 9.8 mS cm^{-1} at room temperature and a single-ion-conducting transference number of 0.92. Computational studies also supported the nine Li^+ mechanism. We used AQ-Si-COF as the solid electrolyte interphase on the Li anode. The LMB cells achieved a maximum reversible capacity of 188 mAh g^{-1} at 0.25 C during high-voltage operation. Moreover, this LMB cell demonstrated suppressed dendrite growth and stable cyclability, with its capacity decreasing by less than 3% over 100 cycles. These findings demonstrate the effectiveness of our redox-active and anionic COFs and that they should have practical utility in LMB-based energy-storage devices.

Full Text

During the past two decades, Li-ion (Li^+) batteries have proven effective for energy storage in various commercial applications, such as portable electronics, electric vehicles, and grid-scale storage.[1] However, as Li^+ batteries have relatively low energy densities, Li-metal batteries (LMBs) have been developed, which have higher energy densities due to their Li metal anodes.[2] LMBs are promising next-generation energy-storage devices as they possess the highest theoretical capacity (3,861 mAh g^{-1}).[3] However, the high reactivity of Li metal with organic solvents results in the formation of dendrites and an unstable and passivated solid electrolyte interphase (SEI), and the connection of dendrites with cathodes causes cell failure .[4] Tremendous efforts have been made to overcome these stability problems.[5, 6] For instance, constructing a stable artificial SEI layer on a Li-metal anode has proven to be an effective strategy because it stabilizes the anode surface and prevents undesirable side reactions between the Li metal and electrolytes, thereby suppressing dendrite growth.[7–9]

An ideal SEI should possess electrochemical, chemical, and mechanical stability, so the above-mentioned problems do not occur, a robust and homogeneous structure to promote the efficient distribution of Li^+ flux, and high Li^+ conductivity (σ_{Li^+}).[10] As Li^+ diffusion and deposition are coupled processes,[11] it is imperative to develop new interphasial chemistry.[12] Sand's theory holds that cation depletion during electrodeposition breaks electrical neutrality and builds up space charge at a plated electrode surface, triggering parasitic reactions that cause metal deposition and thus dendrite formation.[13] In most cases, liquid electrolytes have a low Li^+ transference number (t_{Li^+}), and the majority of their total σ_{Li^+} is

attributable to anion transport. Therefore, the low proportion of the entire ionic conduction by Li^+ results in Li^+ deficiency during cycling.[14–15] Thus, coating a Li-metal anode with electrolyte-based interphases that rapidly and exclusively transport Li^+ effectively prevents both Li^+ depletion and dendrite formation on the anode while maintaining high battery performance.[16–17]

Covalent organic frameworks (COFs) bearing ion-conducting moieties are popular electrolyte-based interphasial materials, as their robustness suppresses dendrite growth while their porosity allows ion conduction.[10,18] For instance, COFs bearing redox-active moieties, such as quinone, can facilitate the transfer of electrons and cations via redox processes (Fig. 1a).[19–23] Dichtel et al. incorporated redox-active 2,6-diaminoanthraquinone moieties into two-dimensional (2D) COFs and found that the resulting COFs exhibited long-term reversible electrochemical processes, excellent chemical stability, and high capacitance.[19] Lu et al. used the same type of β-ketoenamine-linked COFs as Dichtel et al. as the anodes for sodium-ion batteries[20] and found that the anthraquinone radical intermediates enabled stable and high-capacity battery performance. Recently, Tao et al. incorporated pyrene-tetraone-based 2D COFs into aqueous zinc–organic batteries and found that these batteries exhibited a high specific power density (184 kW kg^{-1}) and a reversible capacity (225 mAh g^{-1}) at 0.1 A g^{-1}.[23] Another promising strategy is to introduce ionizable groups into COF backbones to form ionic COFs (Fig. 1a).[24] Coaxially aligned pore channels in ionic COFs have been shown to enable rapid Li^+ conduction through their numerous ionic sites, with exclusive and uniform Li^+ flux that results in high σ_{Li^+}, while also inhibiting dendrite formation.[11, 14, 25–26] The reported room-temperature σ_{Li^+} of these ionic COF electrolytes has reached the order of 1 mS cm^{-1}. By comparison, the imidazolate-based COFs reported by Zhang et al.[25] and Lee et al.[26] have demonstrated the highest room-temperature σ_{Li^+} of 7.2 mS cm^{-1}, which is sufficient for use in solid-state electrolytes. In 2017, Thomas et al. reported the first hexacoordinated 2D silicate COFs; these were formed via a reversible Si–O bond-formation process and thus exhibited crystallinity and high porosity.[27] Recently, Lu et al. used these silicate COFs as the electrolyte interphase for the anode in an LMB and showed that this LMB demonstrated a σ_{Li^+} of 3.7 mS cm^{-1} and a t_{Li^+} of 0.82.[11]

As described above, either redox-active or ionic COFs have been used thus far in batteries. We wondered whether both redox-active and ionic groups could be incorporated into a single COF backbone, and whether these groups would synergistically interact such that the COF would conduct Li^+ and electrons and thus could be used as the solid interphase in LMBs. To investigate this, we developed a simple and effective design for a COF structure bearing both redox-active anthraquinone groups (which also served as the backbone) and anionic silicates (which also served as linkers in the backbone); that is, an anthraquinone silicate COF (AQ-Si-COF). Redox-active 2,3,6,7-tetrahydroxy-9,10-anthraquinone (THAQ) is the building block of AQ-Si-COF, and hypervalent silicates link the anthraquinones to give a structure with three-fold symmetry (Fig. 1b and 1c).

The synthesis of THAQ comprised three steps: first, 9,10-dimethyl-2,3,6,7-tetramethoxyanthracene was obtained by a condensation reaction between 1,2-dimethoxybenzene and acetaldehyde; second, sodium

dichromate was used to oxidize the methyl groups, producing 2,3,6,7-tetramethoxy-9,10-anthraquinone; and finally, demethylation in HBr yielded a brown powder of THAQ. AQ-Si-COFs were then synthesized by a condensation reaction between THAQ and silicon dioxide in methanol, with lithium methoxide added as the Li^+ source. The reaction mixture was heated at 180°C for 4 days, and a dark brown powder of AQ-Si-COFs was obtained in high yield (96%; Figs. 1b and S1–S8; see supporting information for more details). The AQ–Si–COF was then deposited onto a lithium-metal anode to construct an artificial SEI that it was hoped would afford increased electrochemical performance and conductivity while also inhibiting dendrite growth. On the fully Li^+-coordinating repeating unit of AQ-Si-COFs, the ideal discharge processes are completed in two steps. First, six sets of Li^+ and e^- are released from the carbonyl groups, followed by the release of three sets of Li^+ and e^- from the silicates (Fig. 1d and 1e). These release processes are observable by cyclic voltammetry (CV; Fig. 1f); although the fully discharged state may be transient, the structure remains in the form of SiO_6^{2-}, as indicated by previous studies[11, 27] and corroborated by our density functional theory (DFT) calculations. Moreover, these charging steps are fully reversible, which results in selective adsorption and storage of Li^+ from the electrolyte during cycling. Thus, the AQ-Si-COFs SEI can provide an increased theoretical capacity and rate capability for LMBs.

The cyclic voltammograms of AQ-Si-COFs were measured in a 1.5 M lithium hydroxide supporting electrolyte and had four oxidation peaks, at approximately − 0.17 V, 0.54 V, 0.68 V, and 0.84 V, and four reduction peaks, at approximately − 0.21 V, 0.39 V, 0.61 V, and 0.78 V (Fig. 1f). The two main peaks at − 0.17 V and − 0.21 V correspond to the redox reactions that occur around the carbonyl (C = O) groups during the Li^+ insertion/deinsertion processes.[29–30] The peaks near 0.54 V, 0.68 V, 0.84 V, 0.39 V, 0.61 V, and 0.78 V are attributable to electron transfer around the silicates. The peak separation (ΔEp) between the oxidative and reductive waves was small (40 mV), indicating rapid electron transfer between the base electrode and the AQ-Si-COFs SEI.[19] Overall, this shows that the C = O and silicates synergized to provide the largest extent of Li^+ coordination ever reported, thereby enhancing the electrochemical performance of the LMBs. For comparison, we also synthesized silicate COFs from a 9,10-dimethyl-2,3,6,7-tetrahydroxyanthracene (DMA) building block; the resulting DMA-Si-COFs had only anionic groups (Fig. S9).[27] The cyclic voltammogram of DMA-Si-COFs identified four silicate redox peaks: two reduction peaks at 0.05 V and 0.35 V, and two oxidation peaks at 0.18 V and 0.55 V (Fig. S10). Additionally, the cyclic voltammogram of THAQ monomer had peaks at approximately − 0.18 V (oxidation) and − 0.26 V (reduction); this larger ΔEp (≈ 80 mV) was due to the relatively slow heterogeneous charge-transfer process that occurs when THAQ is unmodified (Fig. S11). As expected, our stainless-steel mesh substrate did not exhibit any redox behavior (Fig. S12). Therefore, AQ-Si-COFs had three sets of Li^+ and e^- reversibly interacting with its silicates, whereas only two sets of Li^+ and e^- were observed to reversibly interact with DMA-Si-COF, with the remaining set strongly chemisorbed to its silicates. This is further proof that the more electronegative environment in the AQ-Si-COFs, induced by the C = O and silicates working synergistically, released the last set of Li^+ and e^- through charge interactions. This high-density Li^+ transport mechanism resulted in a high σ_{Li^+} (9.8 mS cm^{-1}) at room temperature and a near-unity single-ion conducting t_{Li^+} (0.92) when AQ-Si-COFs was used an interphase.

Next, we characterized the synthesized AQ-Si-COFs comprehensively. The crystallinity of the framework was determined by powder X-ray diffraction (XRD). The sharp diffraction peaks observed at 4.8° and 8.3° confirmed the crystalline nature of the layered 2D COF structures (Fig. 2a), and similar peaks were found in our DMA-Si-COFs control samples (Fig. S13).[11, 27] Therefore, the quinone group did not affect the formation of the 2D layered COFs, indicating that crystalline 2D layered AQ-Si-COFs were indeed formed via our solvothermal synthesis; otherwise, additional or broadened peaks for other structures would have been present in the XRD pattern. Fourier-transform infrared (FTIR) spectroscopy and solid-state NMR (ssNMR) were used to confirm that no starting materials remained in the product and that the structural integrity of its network was due to the formation of octahedral silicate anions (Fig. 2b, c). FTIR spectra of the THAQ monomer contained characteristic O–H stretching bands (3,200–3,600 cm^{-1}), while those of AQ–Si–COF contained significantly attenuated O–H stretching bands, which confirmed the reaction has gone to completion (Fig. 2b). Moreover, there was a new band in the spectrum of the COFs at 665 cm^{-1}, which was attributed to the Si–O stretching mode in the hexacoordinate silicates. C = O stretching bands were observed at 1,650 cm^{-1} in both COFs and THAQ, confirming the presence of C = O in AQ-Si-COFs. ^{13}C ssNMR spectroscopy of AQ-Si-COFs showed a characteristic peak (labeled peak 4) at ~ 180 ppm, which represents a C = O carbon (Fig. 2c). When the C = O was replaced by a methyl group, as in DMA-Si-COFs, peak 4 significantly shifted to ~ 125 ppm, as the carbon of the methyl group was shielded (Fig. S14). The remaining peaks at 150 ppm (peak 1), 105 ppm (peak 2), and 122 ppm (peak 3) are the carbons of the benzene rings. These spectra contained all the expected peaks, indicating the structural integrity of both COFs. The crystalline morphology of AQ-Si-COFs was observed by scanning electron microscopy (SEM), showing that its particles had an aggregated flower-cluster morphology formed by nanosheets with an approximate thickness of 15 nm (Fig. 2d). The DMA-Si-COF formed similar flower-like nanoplatelets with an approximate thickness of 18 nm (Fig. S15). The porous nature of AQ-Si-COFs were proved by N_2 adsorption isotherm tests, which found a Brunauer–Emmett–Teller surface area of 943 $m^2 g^{-1}$ and an average pore size of 0.7 nm (Fig. 2e).

Furthermore, inductively coupled plasma optical emission spectroscopy found that AQ-Si-COFs contained 3.45 wt% elemental Li, which is close to the calculated value (3.12 wt%). This confirmed that AQ-Si-COFs was a negatively charged organic quinone-based framework complexed with Li^+. In addition, the Li content of DMA-Si-COFs was 2.89 wt%, which was close to its calculated value (3.14 wt%) (Table S1). X-ray photoelectron spectroscopy analyses of AQ-Si-COFs and DMA-Si-COFs were conducted to examine their surfaces (Figs. S16 and S17). The binding energies oft 104.7 eV (Fig. S16b) and 56.2 eV (Fig. S16c) are attributable to the Si 2p orbital in Si–O and the Li 1s orbital in Li–O bonds, respectively. In addition, no Si–Li bond (< 54.4 eV and 98–98.4 eV) was found, indicating the defect-free network nature of AQ-Si-COFs.[11, 38] The detected signals of Si 2p (103.4 eV) and Li 1s (56.1 eV) orbitals in DMA-Si-COFs are consistent with a previous report.[11] The thermal stability of AQ-Si-COFs was also evaluated by thermal gravimetric analysis and showed that it retained high stability without decomposing until 300°C, with a gradual weight loss (~ 43%) observed up to 800°C (Fig. S18).

We next measured the σ_{Li^+} of our samples using electrochemical impedance spectroscopy. The measurement of σ_{Li^+} was carried out in a coin cell configuration, where the sample pellet was fixed between two stainless-steel plates, with impedance measurements conducted at frequencies ranging from 1 Hz to 1 × 10^6 Hz at an amplitude of 100 mV. The σ_{Li^+} of AQ-Si-COFs pellets at room temperature was calculated to be 9.8 mS cm^{-1} (Fig. 2f), with a thermal activation energy of 0.098 eV (Fig. S19). The current–voltage measurements were performed via the Bruce–Vincent–Evans technique (see the supporting information for details)[39] and revealed the t_{Li^+} of AQ-Si-COFs to be 0.92, which is near-unity single-ion conducting behavior (Fig. 2g). These conductivity and transference values are the highest reported among the state-of-the-art examples (Fig. 2h), confirming the synergy between the redox-active and anionic groups in AQ-Si-COFs and demonstrating it has excellent potential for use in electrolyte materials.[11, 25–26, 31–37] By comparison, the σ_{Li^+} at room temperature for DMA-Si-COFs was calculated to be 4.5 mS cm^{-1}, while the t_{Li^+} was 0.86 with an activation energy of 0.14 eV (Figs. S20–S22). The superior values of the AQ-Si-COFs demonstrate that the nine processes of Li^+ sorption/desorption enable effective Li^+ transport during the charging/discharging cycles.

Subsequently, a series of DFT calculations were performed to reveal the atomistic details of the Li^+ transport mechanisms in the AQ-Si-COFs system. For simplicity, one repeated unit from the periodic AQ-Si-COFs was adopted as the representative configuration of the system, with hydrogen termination used to ensure charge neutrality. In addition, the hydrogen atoms and their adjacent carbon atoms were fixed to suppress the flexibility of this isolated unit. Examining this unit's structure, consistent with experiments, two types of Li^+ can be recognized: Li^+ bonded with one oxygen (six Li^+ around the edge of the molecule) and Li^+ shared by two oxygens (three Li^+ close to the center of the molecule). To simulate the ion transport process, we stripped Li^+ from the molecule one cation at a time, starting from the "edge" and moving to the "center," with the system restoring charge neutrality after each Li^+ was stripped. The energy change associated with each ion transport event was contributed to by both the separation of Li^+ from the molecule and the electron removal from the remainder of the molecule. As shown in Fig. 3a, the electron transfer energy exhibited a monotonically increasing trend. The binding energy (defined as $E_b = E^-_{\text{anion}} + E^+_{\text{Li}} - E_{\text{Li-anion}}$, where E_b indicates the binding energy, E^-_{anion} denotes the energy of the structure after losing one Li^+, E^+_{Li} denotes the energy of a single Li^+, and $E_{\text{Li-anion}}$ denotes the energy of the structure before the separation of the charges) showed a general decreasing trend with noticeable fluctuations (Fig. 3b). By combining electron transfer energy with binding energy, the total energy change for each Li^+ stripping is provided (Fig. 3c). Overall, the average increase in total energy at the center (from the seventh Li^+ to the eighth Li^+) is larger than that at the edge (from the first Li^+ to the sixth Li^+). This implies that the inner Li^+ are more stable than the outer Li^+. For instance, the outer Li^+ are bonded to the three branches of the molecule, with each branch having two Li^+ located on either side. Thus, if the Li^+ on one side of this branch is stripped, the structural symmetry is broken, which may destabilize the Li^+ on the other side. This would result in decreases in the energy required to remove the first and second, the third and fourth, and the fifth and sixth Li^+ (Fig. 3c). Regarding the inner Li^+, the detachment of the seventh Li^+

requires relatively little energy, which may be due to steric effects. However, removing the seventh Li^+ leaves space to accommodate the last two Li^+, so these Li^+ are stabilized by the strong nucleophilicity of the SiO_6 group. To better illustrate the electronic properties of the AQ-Si-COFs system, electrostatic potential (ESP) maps were calculated after stripping zero, one, six, seven, eight, and nine Li^+, respectively (Fig. 3d–3i). The nucleophilic regions are colored blue, while the electrophilic regions are colored red. Clearly, the center of the initial structure has a high electron density, leading to a strong affinity for Li^+ (Fig. 3d). With the first Li^+ stripped from the system, the charge distribution becomes asymmetric, promoting the detachment of the other Li^+ on the same branch (Fig. 3e). We also show that the inner Li^+ (and the associated electrons) are removed, the center of the molecule gradually transforms from being nucleophilic to being electrophilic (Fig. 3f–3i). To evaluate the charge evolution of each atom during this ion transport process, Bader charge analyses were performed and are provided in the supporting information (Tables S2–S7 and Figs. S23–S28).

We tested the specific capacity of AQ-Si-COFs and DMA-Si-COFs in a coin-cell setting, where the Si–COFs and Li metal function as the cathode and anode (Si-COFs|Li), respectively, with 1.0 M lithium hexafluorophosphate ($LiPF_6$) in ethylene carbonate/diethyl carbonate (EC/DEC; 50/50 with respect to volume) as the electrolyte. The charge/discharge voltage (Fig. 4a) profiles for AQ-Si-COFs exhibited one main discharge plateau near 2 V, which agrees well with the main reduction peaks of the C = O groups. The practical average capacity reached 380 mAh g^{-1} at a current density of 300 mA g^{-1}; this exceeds the theoretical value of 369.0 mAh g^{-1} (Fig. S29), which is attributed to the porous physical structure enhancing the charge diffusion and storage.[40] AQ-Si-COFs also showed excellent durability over 800 cycles, which were measured at 300 mA g^{-1} in a wide cut-off voltage range (0.01–4.5 V; Fig. 4b). However, DMA-Si-COFs demonstrated a lower capacity with unstable behavior: its measured capacity was 178 mAh g^{-1} (Fig. 4c), while its theoretical capacity was 123.8 mAh g^{-1} (Fig. S30), and the cycling test at a current density of 100 mA g^{-1} showed decreased capacities to approximately 100 mAh g^{-1} after 50 cycles, before increasing to 156 mAh g^{-1} after 100 cycles (Fig. S33). By contrast, the AQ-Si-COFs|Li performed stably over 100 cycles, even at a higher current density of 400 mA g^{-1} (Fig. S34). Similarly, the capacities of AQ-Si-COFs were nearly four times higher than those of DMA-Si-COFs at the same current density: 800, 539, 362, 269, and 212 mAh g^{-1} for the AQ-Si-COFs, and 157, 115, 85, 68, and 55 mAh g^{-1} for the DMA-Si-COFs at current density of 100, 200, 300, 400, and 500 mA g^{-1}, respectively (Figs. 4d, S35, and S36). Remarkably, the capacity of both types of Si-COFs recovered to their initial values when the current density was cycled from initial 100 mA g^{-1} to 500 mA g^{-1} and then back to 100 mA g^{-1}, demonstrating that the Si–COFs possess excellent rate capabilities and stabilities over a wide range of charge/discharge rates.

Given the promising capacity exhibited by AQ-Si-COFs (Fig. 4a–4d), we used AQ-Si-COFs as the SEI on an Li anode, with lithium cobalt oxide ($LiCoO_2$) as the cathode and 1.0 M $LiPF_6$ in EC/DEC (50/50 v/v) as the electrolyte (see the supporting information for the detailed setup). As control experiments, we also prepared $LiCoO_2$|DMA-Si-COFs/Li and $LiCoO_2$|Li to test the effect of redox-active groups and the COFs

SEI, respectively. The voltage window for the cells was set as 3.0–4.4 V (1 C = 180 mA g^{-1}). The galvanostatic charge/discharge performances of cells with an AQ-Si-COFs SEI with thicknesses of 15 μm, 35 μm, and 100 μm, respectively, were evaluated. The 15-μm AQ-Si-COFs SEI cell demonstrated the highest capacity (188 mAh g^{-1}) at 0.25 C, while the 35-μm AQ-Si-COFs SEI cell, 100-μm AQ-Si-COFs SEI cell, and bare Li had capacities of 183 mAh g^{-1}, 98 mAh g^{-1}, and 180 mAh g^{-1}, respectively (Fig. 4e). The 15 μm AQ-Si-COFs SEI cell also showed high capacity, stability, and reversibility in the galvanostatic charge/discharge testing (Fig. 4f), where the AQ-Si-COFs achieved an average discharge capacity of 188 mAh g^{-1} at 0.25 C. The $LiCoO_2$|15-μm-AQ-Si-COFs/Li cell displayed low voltage hysteresis and capacity reduction over 100 test cycles at 0.25 C, which was significantly better than the behavior of the $LiCoO_2$|15-μm-DMA-Si-COFs/Li and $LiCoO_2$|Li cells (Figs. S37 and S38).

During the cycling performance analysis, the $LiCoO_2$|15-μm-AQ-Si-COFs/Li cell demonstrated the highest cyclability, sustaining a 183 mAh g^{-1} capacity (only decreasing by 2.9%) at 0.25 C at 3.0–4.4 V over 100 cycles (Fig. 4g). This performance surpasses the cyclability of most reported $LiCoO_2$ cathodes at a cut-off voltage of 4.4 V. For instance, 6h-surface-modified $LiCoO_2$ samples (6h-LCO) obtained specific charge capacity of 133.8 mAh g^{-1} with a capacity retention of 86.3% at 4.4V after 500 cycles.[41] An outside-in-oriented nanostructured $LiCoO_2$ cathode also achieved a high discharge capacity (177.4 mAh g^{-1}) with 88.8% capacity retention after 100 cycles at a current density of 0.1 C under 4.6V.[42] Additionally, Li-, Al-, and F-modified $LiCoO_2$ delivered a high capacity retention (89.1%) at 185.3 mAh g^{-1} after 100 cycles at an ultrahigh voltage (4.6 V).[43] By comparison, the cell with a 100-μm AQ-Si-COFs SEI displayed a significantly decreasing capacitance from 124 mAh g^{-1} to 31 mAh g^{-1} after 100 cycles. This may be attributable to the thin SEI forming a conformal coating on the Li-metal anode, thereby suppressing interlayer electron self-exchange and increasing the number of active sites available in the 2D-layered COFs.[20] The control sample, $LiCoO_2$|15-μm-DMA-Si-COFs/Li, showed a 65% decrease in capacitance after 100 cycles. The capacity of the cell without a Si–COF coating, $LiCoO_2$|Li, was unstable; it exhibited declining performance and thus had a capacity retention of only 50%. In contrast, even after 200 cycles, the $LiCoO_2$|15-μm-AQ-Si-COFs/Li cell maintained a capacity of 177 mAh g^{-1}, with 94% capacity retention and high coulombic efficiency (~ 99%; Fig. S39). To evaluate the rate performance, different C rates (1 C = 180 mA g^{-1})—0.25 C, 0.4 C, 2 C, 4 C, and 6 C—were applied to the cells. The $LiCoO_2$|15-μm-AQ-Si-COFs/Li cell showed the best rate capability, reaching 103 mAh g^{-1} even at 6 C (Figs. 4h and S40), while the $LiCoO_2$|15-μm-DMA-Si-COFs/Li only achieved 23 mAh g^{-1} at 6 C.

To further investigate the effect of AQ-Si-COFs interphase on dendrite suppression, galvanostatic plating/stripping of Li symmetric cells was performed at a current density of 0.015 mA cm^{-2} over 1 h. The cell with a 15-μm AQ-Si-COFs coating (AQ-Si-COFs/Li|AQ-Si-COFs/Li) maintained ultrastable plating/stripping profiles with a negligible hysteresis (20 mV) without overpotential fluctuation during 1,000 h of testing (Fig. 4i). The cell with a 15-μm DMA-Si-COFs coating (DMA-Si-COFs/Li|DMA-Si-COFs/Li) also showed a relatively small overpotential (40 mV). By contrast, the cell without any Si-COFs

coating (Li|Li) displayed substantial overpotentials (500 mV and 800 mV over 700 h and 980 h, respectively). These tests demonstrated the negligible electrode polarization and excellent interfacial stability between the AQ–Si–COF interphase and the Li-metal electrodes.

Finally, we assessed cross-sectional SEM images of Li anodes from the cycled $LiCoO_2$|15-μm-AQ-Si-COFs/Li, $LiCoO_2$|35-μm-AQ-Si-COFs/Li, $LiCoO_2$|100-μm-AQ-Si-COFs/Li, and $LiCoO_2$|Li cells (100 cycles at 0.25 C). These results corroborated that AQ-Si-COFs SEI stabilized the Li electrodes by keeping their volume constant and suppressing dendrite growth, whereas the volume of bare Li metal expanded by > 5% (Fig. 4j). In terms of the surface morphology (Figs. S41 and S42), the 15-μm and 35-μm AQ-Si-COFs SEIs maintained flat and dense nanosheet morphologies, demonstrating that the SEIs provided a stable and dendrite-free surface during the stripping/plating processes. However, cycled Li metal without any Si-COF coating had a large density of ramified Li deposits (Fig. S41). Furthermore, the 100-μm AQ-Si-COFs SEI displayed a rough morphology because of its comparatively poor electron transfer and adhesion to the Li electrode (Fig. S42). These morphological studies support that an appropriate thickness (~ 15 μm) of AQ-Si-COFs form excellent SEI for high-performance LMBs.

Conclusion

We created innovative 2D COFs, AQ-Si-COFs, that has both redox-active and anionic sites in its porous space. *These redox-active and anionic groups function synergistically, such that AQ-Si-COFs exhibited a* σ_{Li^+} *of 9.8 mS cm*$^{-1}$ *and a single-ion conducting* t_{Li^+} *of 0.92, which are record values* (Fig. 2h). The DFT studies support the existence of a synergistic Li^+ transport mechanism involving the redox-active and anionic sites. The highly conductive and selective Li^+ transporting layers AQ-Si-COFs meant that it exhibited a reversible capacity of 800 mAh g^{-1} at a current density of 100 mA g^{-1}. LMB cells incorporating AQ-Si-COFs as SEI demonstrated an excellent capacity (188 mAh g^{-1} at 0.25 C) and stable cyclabilities (< 3% decrease over 100 cycles) while also suppressing dendrite formation. Overall, we have shown that interphasial chemistry of redox-active and anionic COFs should enable the use 2D COF materials in electrochemical energy-storage devices, thereby establishing a new paradigm for the design of high-performance LMBs.

Declarations

Acknowledgments

This work was supported by the Research Grants Council of the Hong Kong SAR Government (Early Career Scheme, #26309420 and General Research Fund, #16306921 and #16306022) and the Department of Chemical and Biomolecular Engineering, HKUST (startup funding). The supercomputing time was sponsored by the Shanghai Jiao Tong University High-End Computing Center. Y.W. thanks the National Natural Science Foundation of China (No. 52102183, No. 52281240409) and the Natural Science Foundation of Shanghai (No. 22ZR1433400) for their support.

Conflict of Interest

The authors declare no conflict of interest.

References

1. Etacheri, V.; Marom, R.; Elazari, R.; Salitra, G.; Aurbach, D., Challenges in the development of advanced Li-ion batteries: a review. *Energy & Environmental Science* **2011,** *4* (9).
2. Scrosati, B.; Garche, J., Lithium batteries: Status, prospects and future. *Journal of Power Sources* **2010,** *195* (9), 2419-2430.
3. Albertus, P.; Babinec, S.; Litzelman, S.; Newman, A., Status and challenges in enabling the lithium metal electrode for high-energy and low-cost rechargeable batteries. *Nature Energy* **2018,** *3* (1), 16-21.
4. Lin, D.; Liu, Y.; Pei, A.; Cui, Y., Nanoscale perspective: Materials designs and understandings in lithium metal anodes. *Nano Research* **2017,** *10* (12), 4003-4026.
5. Wu, H.; Chen, L.; Chen, Y., A mini-review of advanced separator engineering in lithium metal batteries. *Sustainable Energy & Fuels* **2021,** *5* (22), 5656-5671.
6. Cheng, X. B.; Zhang, R.; Zhao, C. Z.; Zhang, Q., Toward Safe Lithium Metal Anode in Rechargeable Batteries: A Review. *Chem Rev* **2017,** *117* (15), 10403-10473.
7. Ding, F.; Xu, W.; Graff, G. L.; Zhang, J.; Sushko, M. L.; Chen, X.; Shao, Y.; Engelhard, M. H.; Nie, Z.; Xiao, J.; Liu, X.; Sushko, P. V.; Liu, J.; Zhang, J. G., Dendrite-free lithium deposition via self-healing electrostatic shield mechanism. *J Am Chem Soc* **2013,** *135* (11), 4450-6.
8. Wood, S. M.; Pham, C. H.; Rodriguez, R.; Nathan, S. S.; Dolocan, A. D.; Celio, H.; de Souza, J. P.; Klavetter, K. C.; Heller, A.; Mullins, C. B., K+ Reduces Lithium Dendrite Growth by Forming a Thin, Less-Resistive Solid Electrolyte Interphase. *ACS Energy Letters* **2016,** *1* (2), 414-419.
9. Guo, Y.; Niu, P.; Liu, Y.; Ouyang, Y.; Li, D.; Zhai, T.; Li, H.; Cui, Y., An Autotransferable g-C3 N4 Li(+) - Modulating Layer toward Stable Lithium Anodes. *Adv Mater* **2019,** *31* (27), e1900342.
10. Wang, J.; Wang, K.; Xu, Y., Emerging Two-Dimensional Covalent and Coordination Polymers for Stable Lithium Metal Batteries: From Liquid to Solid. *ACS Nano* **2021,** *15* (12), 19026-19053.
11. Li, X.; Tian, Y.; Shen, L.; Qu, Z.; Ma, T.; Sun, F.; Liu, X.; Zhang, C.; Shen, J.; Li, X.; Gao, L.; Xiao, S.; Liu, T.; Liu, Y.; Lu, Y., Electrolyte Interphase Built from Anionic Covalent Organic Frameworks for Lithium Dendrite Suppression. *Advanced Functional Materials* **2021,** *31* (22).
12. Meng, Y. S.; Srinivasan, V.; Xu, K., Designing better electrolytes. *Science* **2022,** *378* (6624), eabq3750.
13. Brissot, C.; Rosso, M.; Chazalviel, J. N.; Lascaud, S., Dendritic growth mechanisms in lithium/polymer cells. *Journal of Power Sources* **1999,** *81-82*, 925-929.
14. Hu, Y.; Wayment, L. J.; Haslam, C.; Yang, X.; Lee, S.-h.; Jin, Y.; Zhang, W., Covalent organic framework based lithium-ion battery: Fundamental, design and characterization. *EnergyChem* **2021,** *3* (1).
15. Diederichsen, K. M.; McShane, E. J.; McCloskey, B. D., Promising Routes to a High Li+ Transference Number Electrolyte for Lithium Ion Batteries. *ACS Energy Letters* **2017,** *2* (11), 2563-2575.

16. Pang, Q.; Liang, X.; Shyamsunder, A.; Nazar, L. F., An In Vivo Formed Solid Electrolyte Surface Layer Enables Stable Plating of Li Metal. *Joule* **2017,** *1* (4), 871-886.
17. Tu, Z.; Choudhury, S.; Zachman, M. J.; Wei, S.; Zhang, K.; Kourkoutis, L. F.; Archer, L. A., Designing Artificial Solid-Electrolyte Interphases for Single-Ion and High-Efficiency Transport in Batteries. *Joule* **2017,** *1* (2), 394-406.
18. Geng, K.; He, T.; Liu, R.; Dalapati, S.; Tan, K. T.; Li, Z.; Tao, S.; Gong, Y.; Jiang, Q.; Jiang, D., Covalent Organic Frameworks: Design, Synthesis, and Functions. *Chem Rev* **2020,** *120* (16), 8814-8933.
19. DeBlase, C. R.; Silberstein, K. E.; Truong, T. T.; Abruna, H. D.; Dichtel, W. R., beta-Ketoenamine-linked covalent organic frameworks capable of pseudocapacitive energy storage. *J Am Chem Soc* **2013,** *135* (45), 16821-4.
20. Gu, S.; Wu, S.; Cao, L.; Li, M.; Qin, N.; Zhu, J.; Wang, Z.; Li, Y.; Li, Z.; Chen, J.; Lu, Z., Tunable Redox Chemistry and Stability of Radical Intermediates in 2D Covalent Organic Frameworks for High Performance Sodium Ion Batteries. *J Am Chem Soc* **2019,** *141* (24), 9623-9628.
21. Zheng, S.; Shi, D.; Yan, D.; Wang, Q.; Sun, T.; Ma, T.; Li, L.; He, D.; Tao, Z.; Chen, J., Orthoquinone-Based Covalent Organic Frameworks with Ordered Channel Structures for Ultrahigh Performance Aqueous Zinc-Organic Batteries. *Angew Chem Int Ed Engl* **2022**, e202117511.
22. Ke, S. W.; Wang, Y.; Su, J.; Liao, K.; Lv, S.; Song, X.; Ma, T.; Yuan, S.; Jin, Z.; Zuo, J. L., Redox-Active Covalent Organic Frameworks with Nickel-Bis(dithiolene) Units as Guiding Layers for High-Performance Lithium Metal Batteries. *J Am Chem Soc* **2022,** *144* (18), 8267-8277.
23. Zheng, S.; Shi, D.; Yan, D.; Wang, Q.; Sun, T.; Ma, T.; Li, L.; He, D.; Tao, Z.; Chen, J., Orthoquinone-Based Covalent Organic Frameworks with Ordered Channel Structures for Ultrahigh Performance Aqueous Zinc-Organic Batteries. *Angew Chem Int Ed Engl* **2022,** *61* (12), e202117511.
24. Liang, X.; Tian, Y.; Yuan, Y.; Kim, Y., Ionic Covalent Organic Frameworks for Energy Devices. *Adv Mater* **2021,** *33* (52), e2105647.
25. Hu, Y.; Dunlap, N.; Wan, S.; Lu, S.; Huang, S.; Sellinger, I.; Ortiz, M.; Jin, Y.; Lee, S. H.; Zhang, W., Crystalline Lithium Imidazolate Covalent Organic Frameworks with High Li-Ion Conductivity. *J Am Chem Soc* **2019,** *141* (18), 7518-7525.
26. Jeong, K.; Park, S.; Jung, G. Y.; Kim, S. H.; Lee, Y. H.; Kwak, S. K.; Lee, S. Y., Solvent-Free, Single Lithium-Ion Conducting Covalent Organic Frameworks. *J Am Chem Soc* **2019,** *141* (14), 5880-5885.
27. Roeser, J.; Prill, D.; Bojdys, M. J.; Fayon, P.; Trewin, A.; Fitch, A. N.; Schmidt, M. U.; Thomas, A., Anionic silicate organic frameworks constructed from hexacoordinate silicon centres. *Nat Chem* **2017,** *9* (10), 977-982.
28. Peng, C.; Ning, G.-H.; Su, J.; Zhong, G.; Tang, W.; Tian, B.; Su, C.; Yu, D.; Zu, L.; Yang, J.; Ng, M.-F.; Hu, Y.-S.; Yang, Y.; Armand, M.; Loh, K. P., Reversible multi-electron redox chemistry of π-conjugated N-containing heteroaromatic molecule-based organic cathodes. *Nature Energy* **2017,** *2* (7).
29. Zhu, L.; Ding, G.; Xie, L.; Cao, X.; Liu, J.; Lei, X.; Ma, J., Conjugated Carbonyl Compounds as High-Performance Cathode Materials for Rechargeable Batteries. *Chemistry of Materials* **2019,** *31* (21), 8582-8612.

30. Kawai, T.; Oyaizu, K.; Nishide, H., High-Density and Robust Charge Storage with Poly(anthraquinone-substituted norbornene) for Organic Electrode-Active Materials in Polymer–Air Secondary Batteries. *Macromolecules* **2015,** *48* (8), 2429-2434.
31. Du, Y.; Yang, H.; Whiteley, J. M.; Wan, S.; Jin, Y.; Lee, S. H.; Zhang, W., Ionic Covalent Organic Frameworks with Spiroborate Linkage. *Angew Chem Int Ed Engl* **2016,** *55* (5), 1737-41.
32. Chen, H.; Tu, H.; Hu, C.; Liu, Y.; Dong, D.; Sun, Y.; Dai, Y.; Wang, S.; Qian, H.; Lin, Z.; Chen, L., Cationic Covalent Organic Framework Nanosheets for Fast Li-Ion Conduction. *J Am Chem Soc* **2018,** *140* (3), 896-899.
33. Guo, Z.; Zhang, Y.; Dong, Y.; Li, J.; Li, S.; Shao, P.; Feng, X.; Wang, B., Fast Ion Transport Pathway Provided by Polyethylene Glycol Confined in Covalent Organic Frameworks. *J Am Chem Soc* **2019,** *141* (5), 1923-1927.
34. Ashraf, S.; Zuo, Y.; Li, S.; Liu, C.; Wang, H.; Feng, X.; Li, P.; Wang, B., Crystalline Anionic Germanate Covalent Organic Framework for High CO2 Selectivity and Fast Li Ion Conduction. *Chemistry* **2019,** *25* (59), 13479-13483.
35. Li, Z.; Liu, Z.-W.; Mu, Z.-J.; Cao, C.; Li, Z.; Wang, T.-X.; Li, Y.; Ding, X.; Han, B.-H.; Feng, W., Cationic covalent organic framework based all-solid-state electrolytes. *Materials Chemistry Frontiers* **2020,** *4* (4), 1164-1173.
36. Li, Z.; Liu, Z. W.; Li, Z.; Wang, T. X.; Zhao, F.; Ding, X.; Feng, W.; Han, B. H., Defective 2D Covalent Organic Frameworks for Postfunctionalization. *Advanced Functional Materials* **2020,** *30* (10).
37. Li, X.; Hou, Q.; Huang, W.; Xu, H.-S.; Wang, X.; Yu, W.; Li, R.; Zhang, K.; Wang, L.; Chen, Z.; Xie, K.; Loh, K. P., Solution-Processable Covalent Organic Framework Electrolytes for All-Solid-State Li–Organic Batteries. *ACS Energy Letters* **2020,** *5* (11), 3498-3506.
38. Liu, F.; Xiao, Q.; Wu, H. B.; Shen, L.; Xu, D.; Cai, M.; Lu, Y., Fabrication of Hybrid Silicate Coatings by a Simple Vapor Deposition Method for Lithium Metal Anodes. *Advanced Energy Materials* **2018,** *8* (6).
39. Evans, J.; Vincent, C. A.; Bruce, P. G., Electrochemical measurement of transference numbers in polymer electrolytes. *Polymer* **1987,** *28* (13), 2324-2328.
40. Kandambeth, S.; Jia, J.; Wu, H.; Kale, V. S.; Parvatkar, P. T.; Czaban-Jóźwiak, J.; Zhou, S.; Xu, X.; Ameur, Z. O.; Abou-Hamad, E.; Emwas, A. H.; Shekhah, O.; Alshareef, H. N.; Eddaoudi, M., Covalent Organic Frameworks as Negative Electrodes for High-Performance Asymmetric Supercapacitors. *Advanced Energy Materials* **2020,** *10* (38).
41. Kim, J.; Kang, H.; Go, N.; Jeong, S.; Yim, T.; Jo, Y. N.; Lee, K. T.; Mun, J., Egg-shell structured LiCoO2 by Cu2+ substitution to Li+ sites via facile stirring in an aqueous copper(ii) nitrate solution. *Journal of Materials Chemistry A* **2017,** *5* (47), 24892-24900.
42. Mao, S.; Shen, Z.; Zhang, W.; Wu, Q.; Wang, Z.; Lu, Y., Outside-In Nanostructure Fabricated on LiCoO(2) Surface for High-Voltage Lithium-Ion Batteries. *Adv Sci (Weinh)* **2022,** *9* (11), e2104841.
43. Qian, J.; Liu, L.; Yang, J.; Li, S.; Wang, X.; Zhuang, H. L.; Lu, Y., Electrochemical surface passivation of LiCoO(2) particles at ultrahigh voltage and its applications in lithium-based batteries. *Nat Commun* **2018,** *9* (1), 4918.

Figures

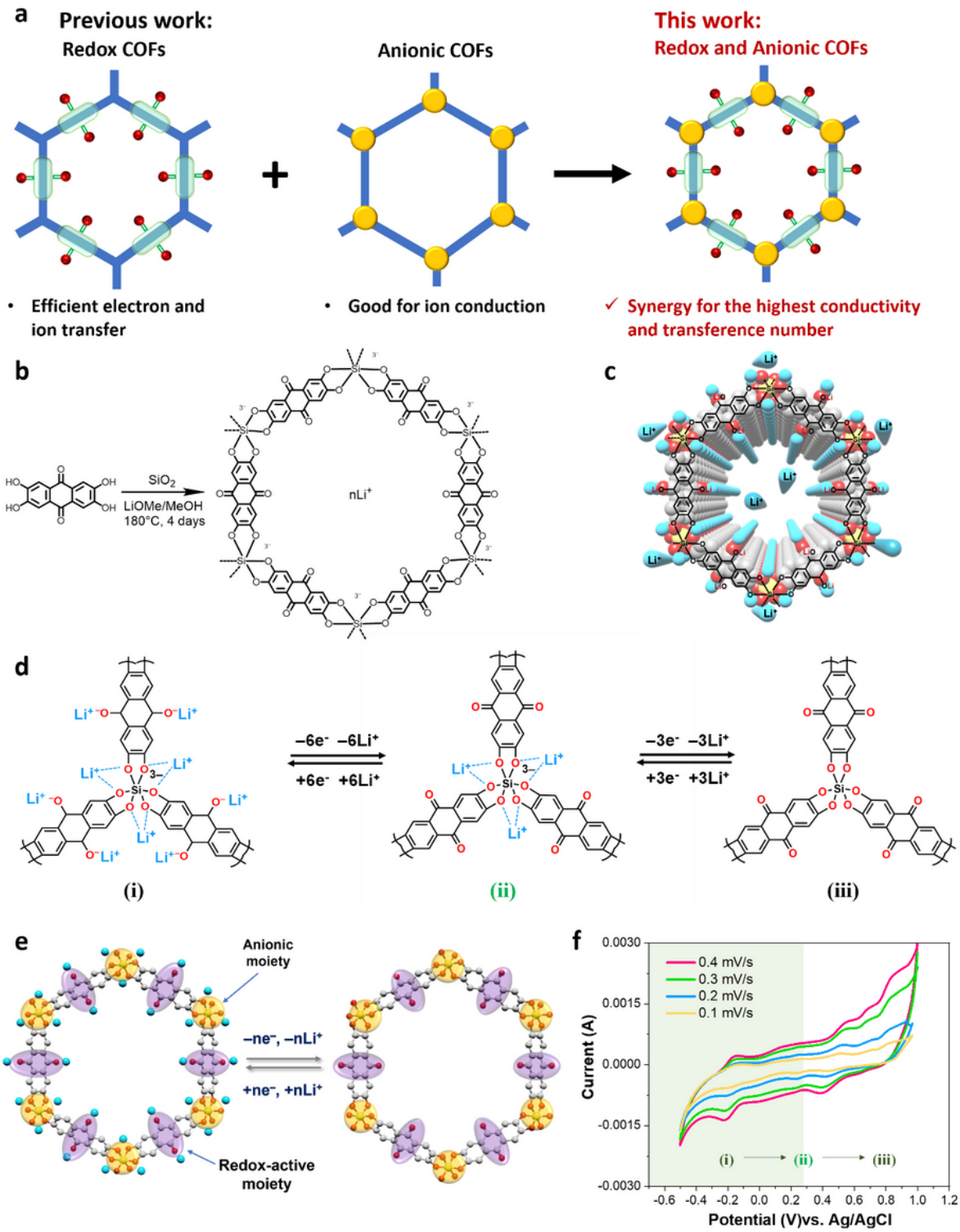

Figure 1

Development of an anthraquinone silicate COF (AQ-Si-COF) that complexes nine Li^+. a, Schematic illustration of previous work, which focused on making either redox-active COFs[20, 22, 28] or anionic

COFs,[11, 26] and this work, which represents the first synthesis of a redox-active and anionic COFs. **b,** Synthesis of the AQ-Si-COFs using reversible Si–O chemistry. **c,** Schematic illustrations of Li^+ transport in the AQ-Si-COFs (blue, yellow, grey, and red represent Li, Si, C, and O, respectively). **d, e,** Schematic showing the complexation of Li^+ and e^- around the AQ–Si–COFs during the charging and discharging processes. **f,** Cyclic voltammograms of the AQ–Si–COFs in solution (1.5 M lithium hydroxide in deionized water).

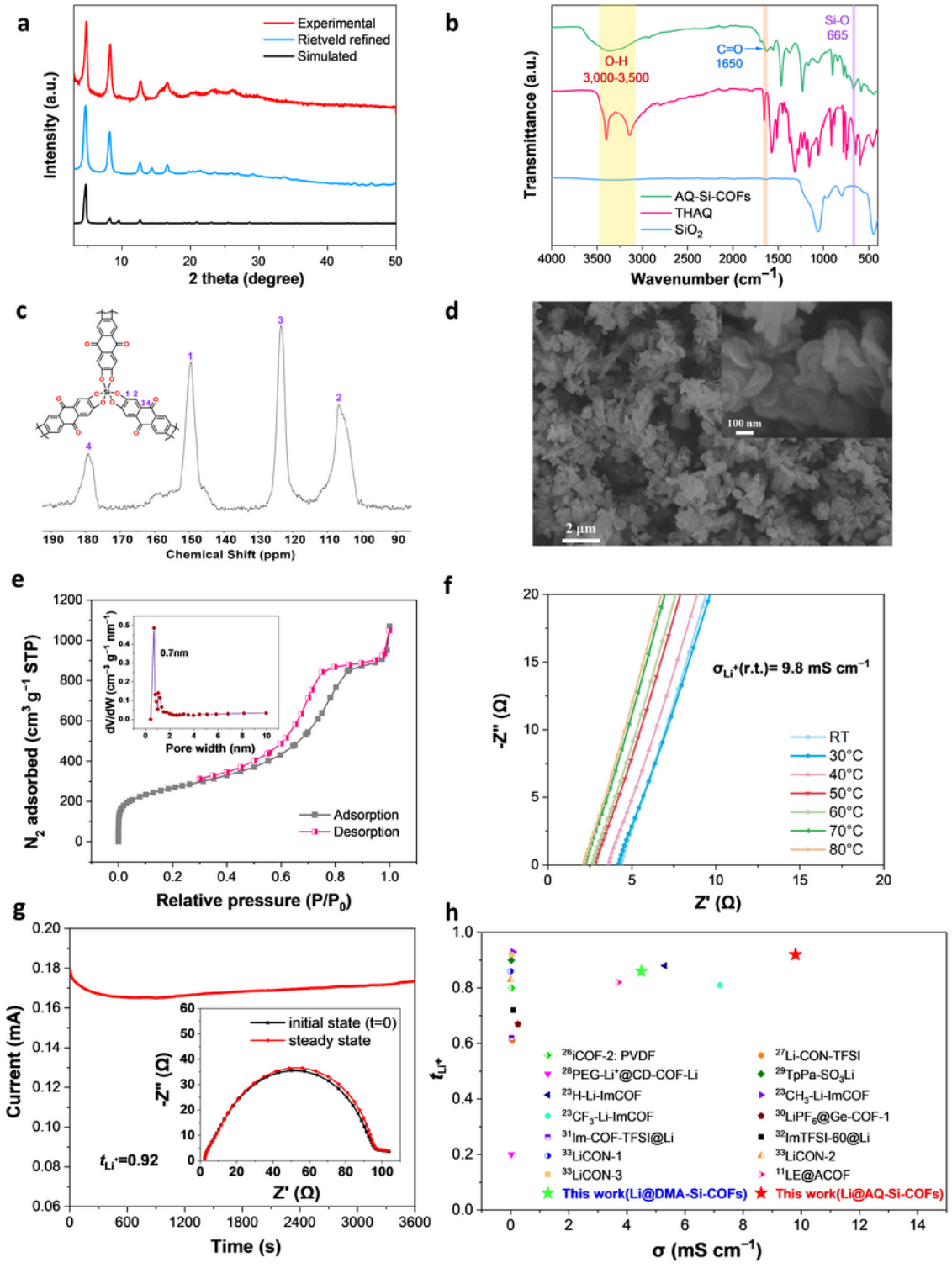

Figure 2

Characterization of AQ-Si-COFs. a–e, Structural features. a, Experimental, Rietveld-refined, and simulated XRD patterns of AQ-Si-COFs. **b,** FTIR spectra of AQ-Si-COFs, THAQ, and silica gel, showing the successful synthesis of AQ-Si-COFs. **c,** Solid-state ^{13}C NMR spectrum of AQ-Si-COFs, showing the structural integrity of its framework. **d,** SEM image of AQ-Si-COFs, showing the formation of uniform platelets. Inset is magnified image of the same sample. **e,** N_2 adsorption/desorption isotherms of AQ-Si-COFs, including an inset with the pore-size distribution data. **f–h, Electrochemical transport. f,** Nyquist plots of AQ-Si-COFs at different temperatures. **g,** t_{Li^+} of AQ-Si-COFs calculated using the Bruce–Vincent–Evans technique. **h,** Comparison chart of σ_{Li^+} and t_{Li^+} for our samples and state-of-the-art values from the recent literature.[11, 25-26, 31-37]

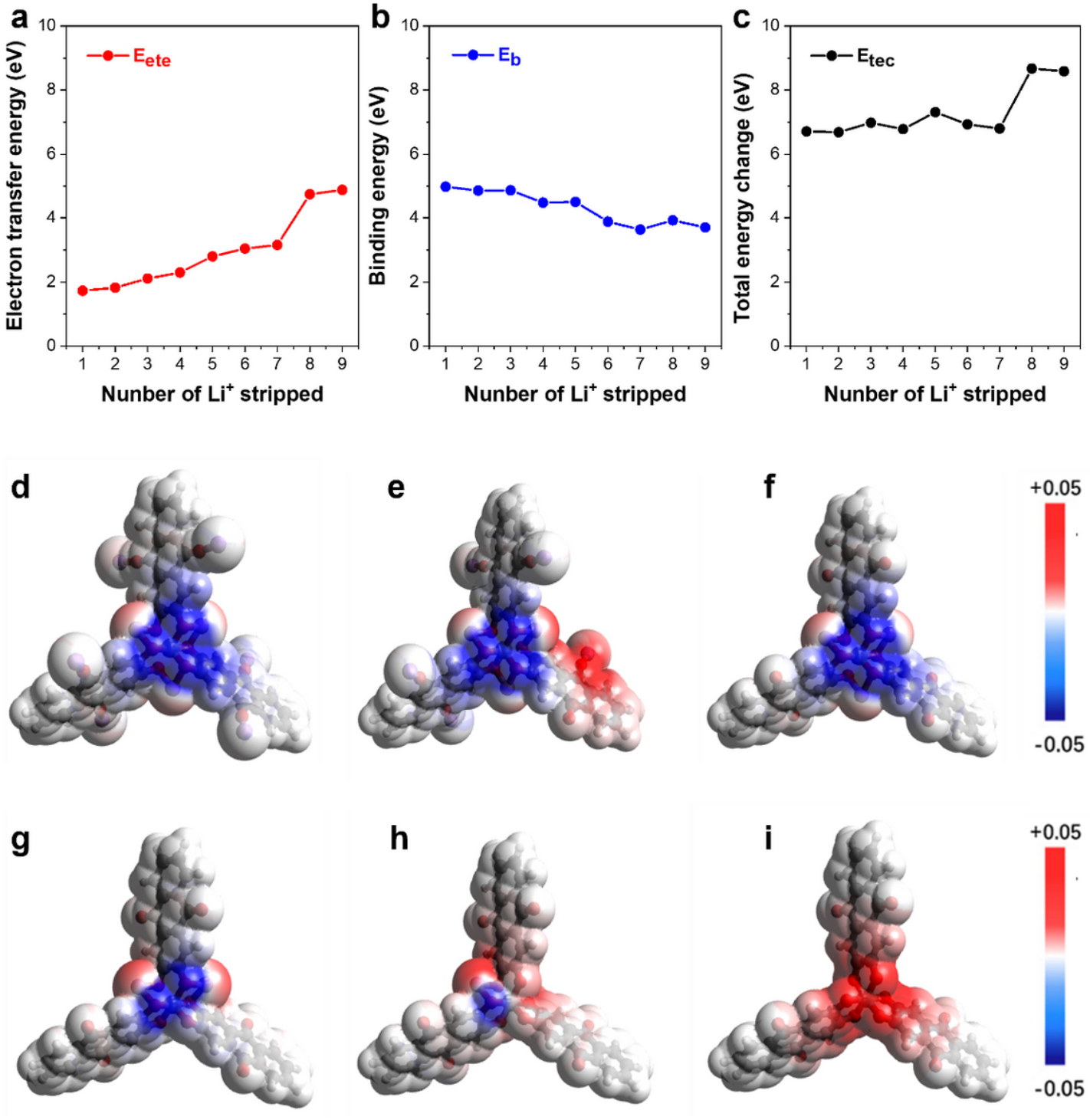

Figure 3

Energy change resulting from sequential Li^+ stripping from AQ-Si-COFs and the corresponding evolution of the ESP maps. a–i, Li^+ removed one at a time from the outside to the inside of AQ-Si-COFs (after each stripping of Li^+, the system is assumed to return to its electrical neutrality). Plots of **a,** the electron transfer energy, E_{ete}, **b,** the binding energy, E_b, and **c**, the total energy change, E_{tec}. **d–i**, the ESP maps of the system after stripping zero, one, six, seven, eight, and nine Li^+, respectively.

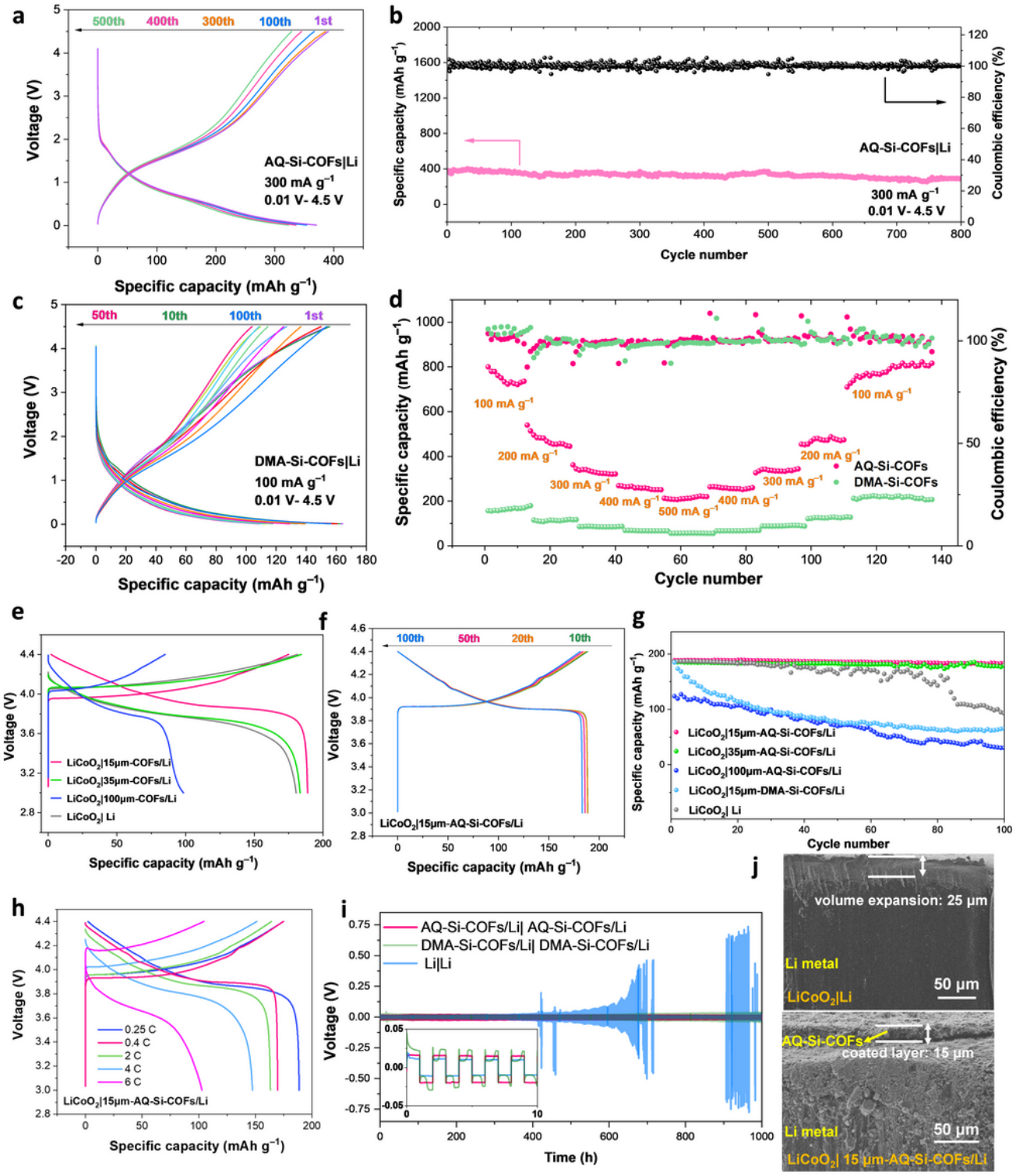

Figure 4

Battery cell tests. a–d, Capacity test of the Si–COFs a, Voltage profiles and **b,** cycle performance an AQ-Si-COFs|Li cell at a current density of 300 mA g^{-1}. **c,** Voltage profiles for the DMA-Si-COFs|Li at a current density of 100 mA g^{-1}. **d,** Comparison of the rate performance of the AQ-Si-COFs|Li, and DMA-Si-COFs|Li cells at current density of 100, 200, 300, 400, and 500 mA g^{-1}. **e–j, Performance of the cells using AQ-Si-**

COFs as SEI. e, Comparison of the voltage profiles for $LiCoO_2$|AQ-Si-COFs/Li with different thicknesses of the COF SEI layers (15 μm, 35 μm, and 100 μm) and $LiCoO_2$|Li upon charge/discharge at 0.25 C. **f,** Voltage profiles of $LiCoO_2$|15-μm-AQ-Si-COFs/Li at 0.25 C. **g,** Comparison of cycle performance of $LiCoO_2$|AQ-Si-COFs/Li with COFs SEI layers of various thicknesses (15 μm, 35 μm, and 100 μm), $LiCoO_2$|15-μm-DMA-Si-COFs/Li, and $LiCoO_2$|Li over 100 cycles. **h,** Representative voltage profiles of $LiCoO_2$|15-μm-AQ-Si-COF/Li at rates of 0.25 C, 0.4 C, 2 C, 4 C, and 6 C. **i,** Galvanostatic cycling at a current density of 0.015 mA cm^{-2} of Li symmetric cells composed of AQ-Si-COFs/Li|AQ-Si-COFs/Li, DMA-Si-COFs/Li|DMA-Si-COFs/Li, and Li|Li. **j,** Cross-sectional SEM image of the Li anode of the cells with and without AQ-Si-COFs coating as an SEI, respectively, after 100 cycles.

Supplementary Files

This is a list of supplementary files associated with this preprint. Click to download.

- AQSiCOFsSI.docx